Computational search for direct band gap silicon crystals

In-Ho Lee,[1,2] Jooyoung Lee,[2,*] Young Jun Oh,[3] Sunghyun Kim,[3] and K. J. Chang[3,†]
[1]*Korea Research Institute of Standards and Science, Daejeon 305-340, Korea*
[2]*Center for In Silico Protein Science, School of Computational Science, Korea Institute for Advanced Study, Seoul 130-722, Korea*
[3]*Department of Physics, Korea Advanced Institute of Science and Technology, Daejeon 305-701, Korea*
(Received 2 March 2014; revised manuscript received 17 September 2014; published 26 September 2014; corrected 1 October 2014)

Due to its abundance, silicon is the preferred solar-cell material despite the fact that current silicon materials have indirect band gaps. Although the band gap properties of silicon have been studied intensively, until now, no direct band gap silicon-based material has been found or suggested. We report here the discovery of direct band gap silicon crystals. By using conformational space annealing, we optimize various crystal structures containing multiple (10 to 20) silicon atoms per unit cell so that their electronic structures become direct band gap. Through first-principles calculations, we identify many direct and quasidirect band gap crystal structures, which exhibit excellent photovoltaic efficiency.

DOI: 10.1103/PhysRevB.90.115209 PACS number(s): 88.40.jj, 42.79.Ek, 71.20.−b, 78.20.Ci

I. INTRODUCTION

Silicon is one of the most abundant elements on Earth, and silicon-based materials can be produced for lower cost than any other semiconductor. For this reason, the most widely used solar-cell materials are all silicon based [1]. Current silicon-based materials, however, have indirect band gaps, and materials with indirect band gaps do not absorb or emit light as efficiently as materials with direct band gaps. Transitions to and from an indirect conduction band only occur via momentum-conserving phonons. Thus silicon solar cells are hundreds of microns thick, while solar cells made from direct band gap materials (such as CdTe, CIGS, or CZTS) can efficiently absorb light even with a very thin (∼1 micron) layer. Also, indirect band gap semiconductors are less likely to absorb light at low temperatures where the phonon populations are low.

Computational methods are revolutionizing the engineering of materials [2]. It is now possible to use computer simulations to design new materials that possess predefined structural and electronic properties. Examples include band gap engineering, alloy design, superconductivity design, and the designing of superhard materials [3–7]. Recently, Botti *et al.* proposed low-energy silicon structures that have quasidirect and dipole-allowed band gaps in the range of 0.8 to 1.5 eV for applications in thin-film solar cells [8]. Also, Xiang *et al.* suggested a quasidirect band gap silicon structure with better optical properties than diamond silicon, the so-called cubic structure Si_{20}-T, containing 20 silicon atoms per simple cubic unit cell [9]. They tried to obtain silicon structures with efficient optical properties, penalizing optically forbidden transitions, by carrying out a conformational search with the particle-swarm optimization algorithm. Yet due to the inefficiency of earlier global optimization methods and the common belief that it is impossible to design a direct band gap silicon-based material, until now no one has identified or suggested a direct band gap silicon-based material, which with a sunlike spectrum would efficiently absorb solar energy.

In this work, we report an approach, which advances design of materials and use it to search for direct band gap silicon crystals. By efficiently exploring the solution space of atomic positions and the shape of crystal unit cell, we find many stable direct band gap crystalline silicon structures. Calculations based on quantum mechanics show that the optical properties of the designed crystals with direct and quasidirect band gaps are more efficient than those of indirect band gap structures, demonstrating that our approach is superior to the existing methods.

II. METHODS

The goal of computational materials design is to find materials with specific desirable properties, and many scientists have proposed to solve the inverse problem of materials characterization [3–6]. In our case, we search for a crystalline silicon phase with a direct band gap in its electronic structure. Potential candidate structures can be generated either in a random fashion or in a grid search for small systems. However, as shown in the Lennard-Jones cluster problem, the number of local energy minima of a combinatorial optimization problem typically scales exponentially with system size [10,11], and so the aforementioned search methods do not work properly for medium to large size problems. Therefore, to draw meaningful conclusions from a computational materials design study, one should start with the energy landscape of the intended material represented as accurately as possible, and then explore the landscape by applying the best available sampling strategy. For sampling, we use conformational space annealing (CSA) to generate many distinct low-energy silicon crystals with direct band gaps. CSA has been successfully applied to various difficult combinatorial optimization problems including protein structure prediction [11–14]. Here, we develop a variant of the CSA algorithm for inverse band structure design [3], in which we optimize the crystalline silicon structure through the enthalpy minimization by using first-principles calculations, and use its electronic structure, also calculate in the *ab initio* fashion, for the selection of direct band gap solutions.

The details of CSA are given elsewhere [11,12], but here we provide a brief description. To apply CSA, three ingredients are needed: a local minimizer, a way to generate a daughter

*Corresponding author: jlee@kias.re.kr
†Corresponding author: kjchang@kaist.ac.kr

TABLE I. For each structure, the lattice type, the number of atoms per unit cell, the volume per atom, the energy per atom relative to diamond Si, the direct gap size (E_g^d), and the indirect gap size (E_g^i) are shown, based on the PBE calculations. Lattice types are abbreviated, such as tc: triclinic, bcm: base-centered monoclinic, or: orthorhombic, pm: primitive monoclinic, bct: body-centered tetragonal, sc: simple cubic, bcc: body-centered cubic, rho: rhombohedral, and fcc: face-centered cubic. Q135 is classified as a quasidirect gap semiconductor according to the quasiparticle calculation, while it is of direct gap according to the PBE functional. All eight direct gap structures shown in the top eight rows are confirmed as direct gap semiconductors in both calculations.

Structure	Lattice	Atoms	(Å^3/atom)	(eV/atom)	$\overline{r}$ (Å), σ_r (Å)	$\overline{\theta}$ (°), σ_θ (°)	E_g^d (eV)	E_g^i (eV)	Space group	Ref.
D262	pm	10	21.02	0.08	2.37, 0.04	109.26, 8.17	**0.29**		$P2_1/m$ (*No.* 11)	
D12	or (C)	10	21.56	0.13	2.37, 0.01	108.98, 11.19	**0.50**		$Cmmm$ (*No.* 65)	
D239	tc	10	22.72	0.16	2.37, 0.03	108.69, 13.50	**0.77**		$P1$ (*No.* 1)	
D63	bcm	12	21.10	0.12	2.37, 0.04	109.09, 9.76	**0.66**		$C2/m$ (*No.* 12)	
D135	bcm	12	21.24	0.22	2.38, 0.05	108.42, 14.73	**0.64**		Cc (*No.* 9)	
D243	tc	12	21.88	0.29	2.38, 0.04	107.29, 18.42	**0.61**		$P1$ (*No.* 1)	
D76	bcm	20	21.70	0.13	2.37, 0.03	109.01, 10.59	**0.57**		$C2$ (*No.* 5)	
D979	tc	20	21.17	0.29	2.38, 0.05	108.56, 18.40	**0.60**		$P1$ (*No.* 1)	
Q130	bcm	12	21.86	0.08	2.37, 0.02	108.97, 9.78	0.64	**0.63**	$C2/m$ (*No.* 12)	
Q135	bcm	12	21.50	0.15	2.37, 0.04	108.95, 11.78	**0.93**		$C2/c$ (*No.* 15)	
Q465	tc	12	21.85	0.13	2.37, 0.02	109.06, 13.63	1.25	**1.23**	$P\bar{1}$ (*No.* 2)	
Q1102	pm	12	21.55	0.14	2.37, 0.02	109.19, 13.97	1.33	**1.20**	Pc (*No.* 7)	
Q419	tc	12	22.25	0.20	2.38, 0.03	108.71, 14.11	1.26	**1.11**	$P1$ (*No.* 1)	
Q8	tc	14	20.35	0.30	2.39, 0.05	108.84, 17.19	0.65	**0.56**	$P1$ (*No.* 1)	
Q57	tc	14	21.55	0.34	2.39, 0.05	107.77, 18.95	0.34	**0.23**	$P1$ (*No.* 1)	
Q1377	tc	16	21.15	0.28	2.39, 0.05	108.23, 14.43	0.34	**0.26**	$P1$ (*No.* 1)	
Q913	tc	18	20.83	0.26	2.38, 0.05	108.56, 16.63	0.91	**0.77**	$P1$ (*No.* 1)	
Q833	tc	18	20.94	0.26	2.38, 0.03	108.07, 15.59	0.73	**0.69**	$P1$ (*No.* 1)	
Q1023	tc	18	20.37	0.28	2.40, 0.06	106.15, 17.60	0.30	**0.17**	$P1$ (*No.* 1)	
Q50	tc	18	20.54	0.31	2.39, 0.06	108.82, 17.99	0.51	**0.41**	$P1$ (*No.* 1)	
Q78	or	20	21.64	0.11	2.37, 0.01	109.26, 11.42	0.74	**0.69**	$Pma2$ (*No.* 28)	
Q636	tc	20	20.89	0.15	2.38, 0.04	109.09, 10.79	0.96	**0.84**	$P1$ (*No.* 1)	
Q736	tc	20	20.89	0.16	2.37, 0.04	109.26, 11.07	0.92	**0.78**	$P1$ (*No.* 1)	
Q85	tc	20	20.11	0.21	2.38, 0.05	109.13, 13.15	0.69	**0.58**	$P1$ (*No.* 1)	
Q202	tc	20	20.13	0.22	2.38, 0.05	109.41, 12.55	0.47	**0.43**	$P1$ (*No.* 1)	
Q7	tc	20	20.43	0.22	2.38, 0.05	109.16, 13.38	0.54	**0.44**	$P1$ (*No.* 1)	
Q108	tc	20	21.19	0.23	2.38, 0.05	108.74, 13.74	0.69	**0.67**	$P1$ (*No.* 1)	
Q660	tc	20	20.95	0.30	2.39, 0.06	106.53, 18.76	0.34	**0.31**	$P1$ (*No.* 1)	
I391	pm	12	22.29	0.12	2.37, 0.02	109.15, 11.31	1.09	**0.91**	$P21/m$ (*No.* 11)	
I512	pm	12	22.61	0.16	2.37, 0.02	108.65, 12.58	1.12	**0.95**	Pm (*No.* 6)	
I241	pm	12	18.33	0.18	2.39, 0.01	108.48, 16.45	1.08	**0.85**	$P21/c$ (*No.* 14)	
I1373	bct	14	21.73	0.06	2.37, 0.02	109.19, 8.30	1.66	**1.29**	$I\bar{4}$ (*No.* 82)	
I713	tc	14	21.67	0.26	2.38, 0.05	108.62, 14.78	0.75	**0.43**	$P1$ (*No.* 1)	
I844	tc	14	20.99	0.28	2.38, 0.04	107.76, 18.10	0.86	**0.70**	$P1$ (*No.* 1)	
I926	bcm	16	21.47	0.07	2.37, 0.02	109.32, 7.80	1.31	**1.10**	$C2/m$ (*No.* 12)	
I1229	tc	16	20.61	0.11	2.37, 0.04	109.20, 9.18	0.89	**0.62**	$P\bar{1}$ (*No.* 2)	
I1233	tc	16	20.76	0.16	2.37, 0.03	108.84, 10.93	1.00	**0.69**	$P1$ (*No.* 1)	
I671	tc	18	20.68	0.14	2.38, 0.04	109.21, 10.68	1.34	**0.97**	$P1$ (*No.* 1)	
I617	tc	18	21.22	0.23	2.38, 0.04	108.99, 15.13	0.56	**0.38**	$P1$ (*No.* 1)	
I83	tc	18	20.65	0.25	2.38, 0.05	108.93, 15.16	0.79	**0.50**	$P1$ (*No.* 1)	
I16	pm	20	20.72	0.12	2.37, 0.04	109.23, 9.30	0.92	**0.68**	$P2_1$ (*No.* 4)	
I257	tc	20	20.58	0.16	2.38, 0.04	109.20, 10.96	0.80	**0.63**	$P1$ (*No.* 1)	
Si_{20}-T	sc	20	21.35	0.29	2.36, 0.01	109.03, 19.02	0.99	**0.97**	$P2_13$ (*No.* 198)	[9]
$NaSi_6$ w/o Na	or	12	21.97	0.09	2.37, 0.01	109.00, 10.08	**0.58**	0.50	$Cmcm$ (*No.* 63)	[22]
Si-III (BC8)	bcc	8	18.44	0.16	2.38, 0.02	108.23, 9.52		−0.12	$Ia\bar{3}$ (*No.* 206)	[23]
Si-XII (R8)	rho	8	18.20	0.16	2.38, 0.02	107.67, 13.02		−0.28	$R\bar{3}$ (*No.* 148)	[24]
clathrate-I	sc	46	23.24	0.06	2.37, 0.01	109.34, 5.07	1.312	**1.307**	$Pm\bar{3}n$ (*No.* 223)	[25]
a-Si				0.28	2.38, 0.08	108.32, 15.5				[26]
a-Si				0.25	2.35, 0.09	108.64, 14.04				[27]
a-Si						108.6, 11.3				[28]
diamond Si										
calc.	fcc	2	20.46	0.00	2.37, 0.00	109.47, 0.00	2.56	**0.62**	$Fd\bar{3}m$ (*No.*227)	
expt.			20.01				3.40	**1.17**		[29]

solution from one or two parent solution(s), and finally, a measure to estimate the difference between two solutions. CSA follows multiple trajectories of local minima and, in a broad sense, belongs to the genetic algorithm category [15]. The immediate goal of CSA is to generate many distinct low-energy local minima, and special care is applied to control the diversity of the sampled population. Annealing is performed in an abstract solution space, so that in the early stage of the algorithm, diversity of the population is kept rather high, and in later stages, low-energy and yet diverse solutions are kept. The key difference of the current sampling approach from the usual CSA is that enthalpy minimization is performed while the objective function for the CSA procedure is the band gap size of the electronic structure.

The simple objective function used in this study is $-E_g^i + \max[0,(E_g^d - E_g^i)]$, where the direct and indirect band gap sizes in the electronic structure are denoted by E_g^d and E_g^i, respectively. It is easy to anticipate that the objective function favors a large indirect band gap and simultaneously a small direct band gap. For a given number of silicon atoms ($n = 10$, 12, 14, 16, 18, and 20) per unit cell, the degrees of freedom include the set of silicon atomic positions $\{\vec{R}_I\}$ and six lattice parameters (a, b, c, α, β, and γ). The volume of the unit cell is allowed to fluctuate by as much as 12% from its theoretical value in diamond silicon, namely 20.46 Å^3/atom.

Suppose we want to explore the conformational space of a silicon crystal with $n = 12$ atoms. CSA starts with $N = 20$ conformations, which are randomly generated in the unit cell. Each conformation is then subjected to a subsequent local minimization procedure (the first ingredient of CSA, see above). For given ionic positions, the enthalpy of the system is minimized at zero pressure by performing density functional calculations, [16] which employ the functional form of Perdew, Burke, and Ernzerhof (PBE) [17] for the exchange-correlation potential and the projector augmented wave potentials [18] as implemented in the VASP code [19]. Using a $\vec{k}$-point mesh with a grid spacing of $2\pi \times 0.02$ Å^{-1}, we repeat the iterative procedure until all the forces and stress tensors are less than 0.01 eV/Å and 1.5 kbar, respectively. When the ions are repositioned, the electronic structure is recalculated, which again affects the ionic positions and lattice parameters, and so on. To avoid core-core repulsion between the ions, special care must be paid to prevent a situation where two ions come too close to each other, which may ruin the quantum computation by causing an anomalous divergence. Prior to each first-principles calculation, unfavorable ionic positions causing core-core overlap are adjusted by performing short Monte Carlo simulations [20], where the maximum size of positional perturbation is set to one-half of the Wigner-Seitz radius.

For the second ingredient of CSA, mutation and crossover are carried out to generate daughter conformations. Crossover is performed in the same manner as CSA was applied to Lennard-Jones clusters [11]. All daughter conformations are subsequently minimized as described above. As the distance measure between two given solutions (the final ingredient of CSA), we use the square root of the Hamming distance between two vectors, where vectors represent the sorted bond lengths between silicon atoms. Bond lengths are generated from the crystal structure constructed by $2 \times 2 \times 2$ expansion of the unit cell.

The key CSA procedure is as follows: at each stage, $N = 20$ locally minimized solutions constitute the sampling population. For each newly generated daughter solution σ, out of $N = 20$ current populations, the closest one to σ is identified, which is called Σ. If the distance between σ and Σ ($D_{\sigma\Sigma}$) is less than the current annealing parameter D_{cut}, σ is considered to be similar to Σ, and σ can replace Σ if it is better in the objective function value (otherwise σ is discarded). But, if $D_{\sigma\Sigma} \geqslant D_{\text{cut}}$, σ can replace the worst objective function value solution in the population. It is easy to picture that the diversity of the sampling population can be controlled by D_{cut}. We set D_{cut} to a large value in the early stages of the procedure, and then gradually reduce it to smaller values. For each minimized solution, first-principles electronic structure calculations are performed to accurately estimate the band gap sizes (E_g^d and E_g^i) and then obtain the objective function value, which is used in the above CSA procedure. In this case, Kohn-Sham eigenvalues [21] are calculated on the high resolution $\vec{k}$-point mesh with grid spacings of $2\pi \times 0.01 \sim 2\pi \times 0.02$ Å^{-1},

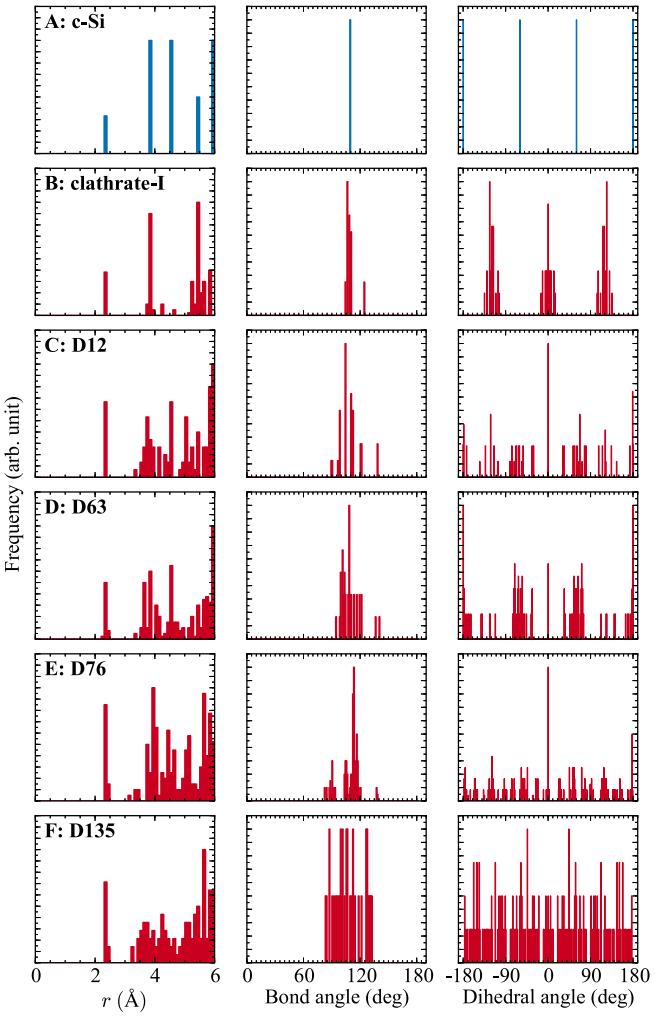

FIG. 1. (Color online) Bond length, bond angle, and dihedral angle distributions are shown for cubic diamond, clathrate-I, D12, D63, D76, and D135.

corresponding to about 1000 $\sim$ 2000 $\vec{k}$ points in the irreducible Brillouin zone.

III. RESULTS AND DISCUSSION

Considering up to $n = 20$ atoms in a unit cell, without using any specific knowledge of other existing silicon crystalline structures, we obtain many promising low-energy metastable structures, including eight direct gap crystals and 20 quasidirect gap crystals ($E_g^i < E_g^d \leqslant E_g^i + 0.15$ eV), as shown in Table I. The optical properties of some of them are found to be excellent, as will be discussed later. For comparison, the previously proposed structure of Si_{20}-T with a quasidirect band gap [9], amorphous silicon (experiment and calculation), and experimentally observed silicon structures including cubic diamond are also given. Note that the six newly designed direct gap structures are all energetically more stable than Si_{20}-T and amorphous silicon.

When bond length, bond angle, and dihedral angle distributions are calculated, we observe that many designed silicon structures are superior to Si_{20}-T and amorphous silicon in terms of local geometry, with smaller deviations of bond lengths and bond angles from their ideal values. In fact, we find that the total energy with respect to diamond silicon can be well fitted to $\Delta E = p\sigma_r + q\sigma_\theta$ with $p = 1.43$ eV/Å and $q = 0.0108$ eV/deg, showing that the excess energy arises mostly from the bond angle deviation from its ideal value. The dihedral angle, on the other hand, is distributed rather broadly, like an almost flat distribution. An analysis of the newly discovered silicon crystal structures, in terms of coordination numbers, bond lengths, bond angles, dihedral angles (Figs. 1 and 2), shows that they are semiconductors with stable local geometries and strong covalent bonds. We point out that the predicted structures are all crystalline, with well-defined space

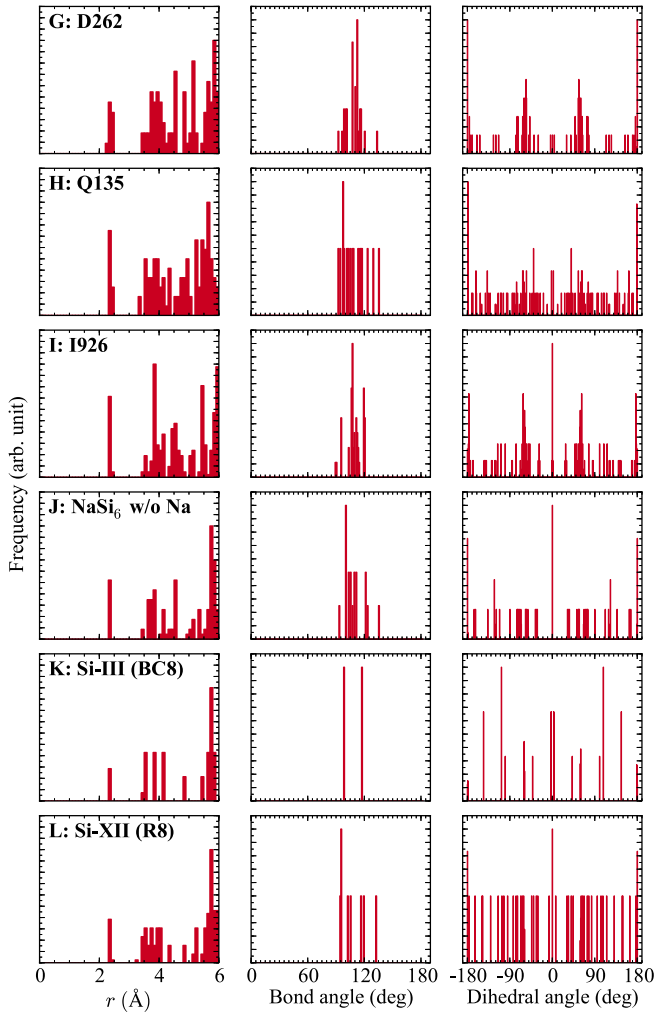

FIG. 2. (Color online) Bond length, bond angle, and dihedral angle distributions are shown for D262, Q135, I926, $NaSi_6$ clathrate without Na (Ref. [22]), Si-III (BC8), and Si-XII (R8).

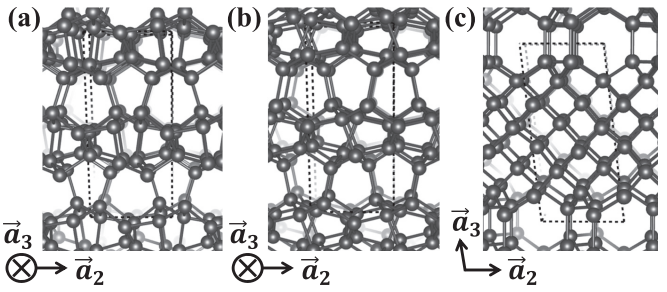

FIG. 3. Atomic structures of (a) D135, (b) Q135, and (c) I926 are shown. No coordination defects are found.

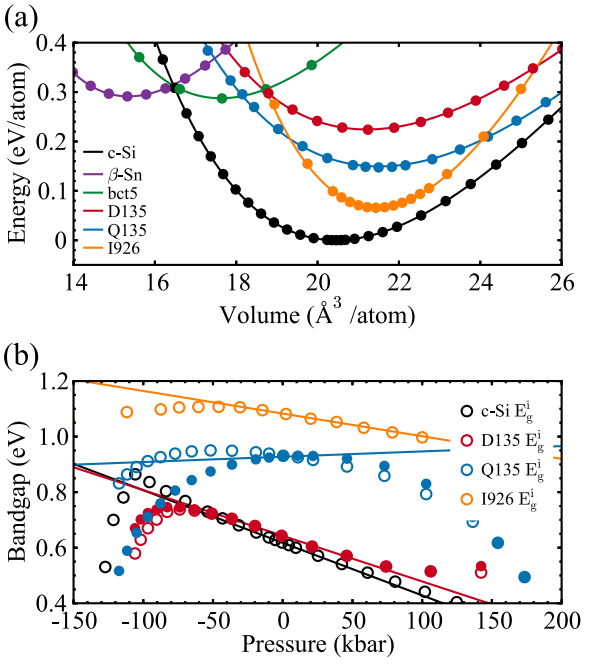

FIG. 4. (Color online) (a) Total energy (eV/atom) vs atomic volume curves plotted for cubic diamond, β-Sn, bct5, D135, Q135, and I926. (b) The characteristic band gap size dependence on the external pressure is shown for D135, Q135, I926, and diamond Si. D135 undergoes a transition from direct band gap to indirect band gap at pressures above 106 kbar. Also, at pressures below -51 kbar, D135 becomes indirect. Black symbols represent the indirect band gap of diamond Si, which decreases more rapidly than D135 as pressure increases.

groups by 10 to 20 silicon atoms in the unit cell (Table I). Moreover, they exhibit very sharp peaks in the distribution of bond lengths due to the fourfold coordination, while the bond-length distribution is broad and coordination defects exist in the amorphous Si.

Relating to the structural and optical properties, we focus on the three structures, D135, Q135, and I926, which have the direct, quasidirect, and indirect gaps, respectively. These structures contain no coordination defects, but do have slightly distorted tetrahedral bonds, as shown in Fig. 3. The amounts of distortions are represented by the deviations of bond lengths and bond angles from their ideal values (Table I). Due to the bond angle fluctuation ($\sigma_\theta = 14.73^\circ$, 11.78°, and 7.80° for D135, Q135, and I926, respectively), the internal energies of D135, Q135, and I926 are higher by 0.22, 0.15, and 0.07 eV/atom, respectively, compared with diamond Si, but lower than those for β-Sn, body-centered tetragonal 5 (bct5) [30], and amorphous Si (Fig. 4 and Table I). The lattice mismatches of direct gap silicon crystals with diamond Si are all rather small (1% $\sim$ 4% in Table I), especially, only off by 1.3% for D135 and 1.7% for Q135.

As mentioned earlier, the enthalpy is minimized to find target structures, which only warrants that the obtained structures are stable at zero temperature. For this reason, we examine

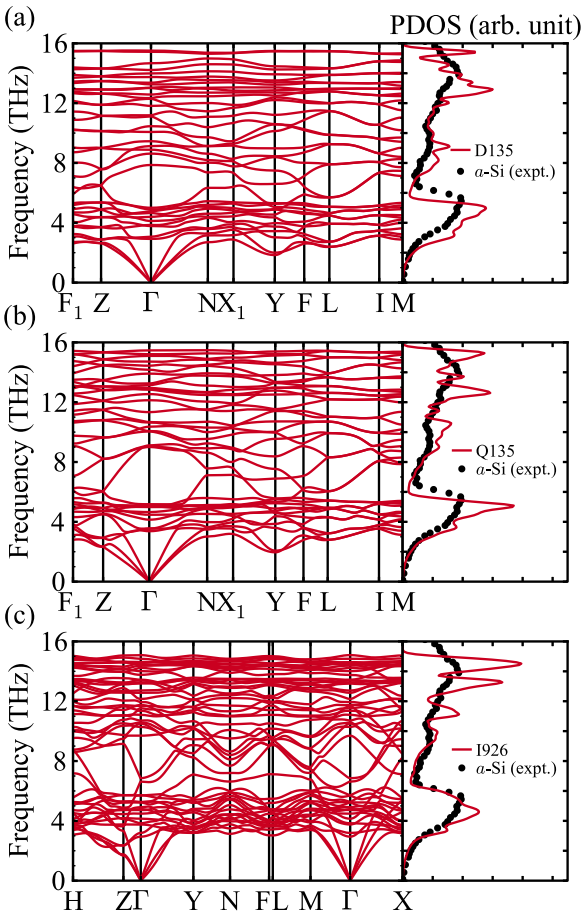

FIG. 5. (Color online) The phonon dispersion and phonon density of states are shown for (a) D135, (b) Q135, and (c) I926. The phonon density of states of amorphous Si ($a-$Si) is taken from Ref. [32].

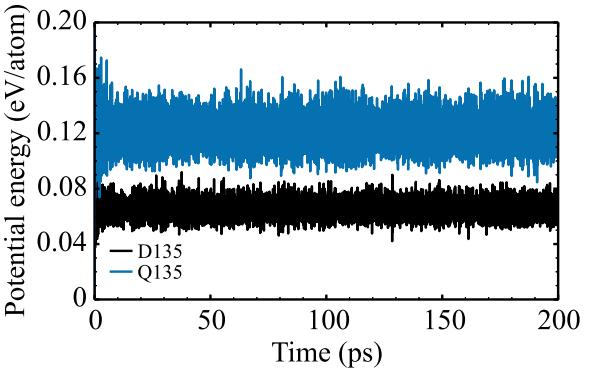

FIG. 6. (Color online) The thermal stability of D135 and Q135 is examined by performing first-principles molecular dynamics simulations for 200 ps at temperatures 500 and 900 K for D135 and Q135, respectively. Potential energy fluctuations are obtained for a supercell containing 96 atoms (eight unit cells).

the structural stability of D135 and Q135 at the ambient condition in two ways. First, we carry out first-principles lattice dynamics calculations [31]. To calculate the dynamical matrix, we use a sufficiently fine-meshed grid so that the sum rule is not needed to correct errors in atomic forces. The phonon density of states is calculated by using the $\vec{k}$-points generated by the $20 \times 20 \times 20$ mesh. The phonon spectra of D135 and Q135 display no imaginary phonon modes in the Brillouin zone (Fig. 5). Secondly, we perform first-principles

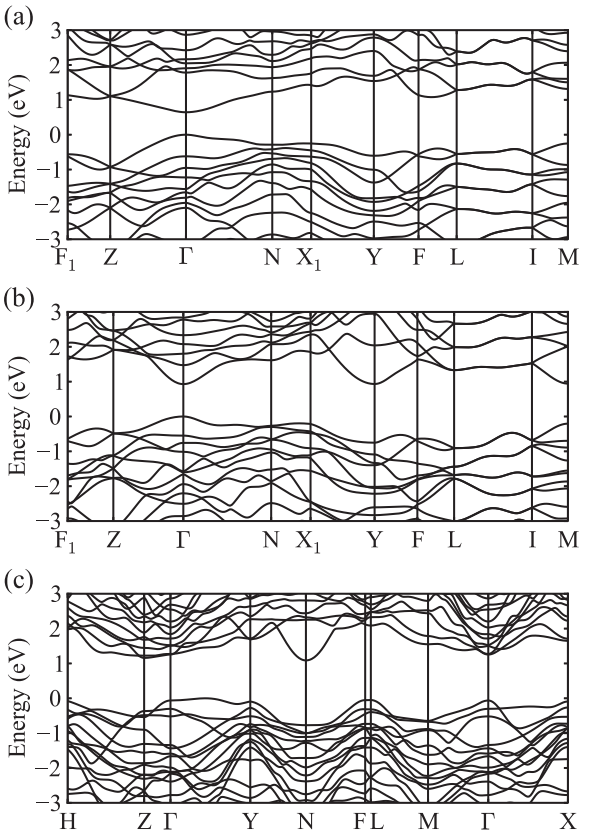

FIG. 7. The PBE electronic band structures of (a) D135, (b) Q135, and (c) I926 are shown near the Fermi level. The Bravais lattices of D135, Q135, and I926 are base-centered monoclinic.

TABLE II. The estimated photovoltaic parameters for eight designed silicon crystal structures are listed. The optical type, the band gap, the fraction of radiative electron-hole recombination current parameter (f_r), the film thickness (L), the open circuit voltage (V_{oc}), the voltage at the maximum power (V_{max}), and the spectroscopic limited maximum efficiency (SLME) [38] are shown. Here, $E_g^d(G_0W_0 - \text{BSE})$ and $E_g^{op}(G_0W_0 - \text{BSE})$ denote the direct transition gap and the optically allowed transition gap in the G_0W_0 and BSE calculations, respectively.

Structure	Type	$E_g^d(G_0W_0 - \text{BSE})$(eV)	$E_g^{op}(G_0W_0 - \text{BSE})$(eV)	f_r	$L(\mu\text{m})$	V_{oc}(V)	V_{max}(V)	SLME(%)
D135	OT1	0.98	0.98	1	0.5	0.75	0.67	29.71
D63	OT1	1.01	1.01	1	0.5	0.78	0.69	29.17
Q130	OT3	1.01	1.01	0.80	0.5	0.78	0.69	26.64
Q135	OT3	1.33	1.33	2.6×10^{-2}	0.5	0.99	0.89	29.77
I926	OT3	1.68	1.68	8.9×10^{-6}	0.5	1.10	1.01	22.37
Q465	OT4	1.69	1.70	6.3×10^{-2}	0.5	1.34	1.24	22.32
Q1102	OT3	1.70	1.70	2.4×10^{-3}	0.5	1.26	1.17	25.29
Q419	OT3	1.64	1.64	2.2×10^{-3}	0.5	1.20	1.10	26.38
Q78	OT3	1.06	1.06	0.18	0.5	0.71	0.63	25.70
Q636	OT3	1.31	1.31	4.5×10^{-3}	0.5	0.92	0.83	28.02

molecular dynamics simulations at temperatures 400∼900 K. We observe that D135 is stable over 200 ps at 500 K, much higher than the usual solar-cell operating temperature, with atomic fluctuations within 0.176 ± 0.077 Å (Fig. 6). D135 is observed also quite stable up to about 80 ps at 800 K, but the structure is transformed into Q135 with the slightly lower energy (Table I). The structural change is involved with breaking two long Si–Si bonds (2.49 Å) in proximity and reforming two shorter bonds (2.46 Å) in the primitive unit cell, and the final atomic structure of Q135 is quite similar to that of D135. Moreover, when molecular dynamics simulations are performed at the high temperature of 900 K, Q135 is found to be stable up to 200 ps, which is much longer than previous simulation times of ∼10 ps [9].

The band gap variation against external pressure is shown for D135, I926, and diamond silicon in Fig. 4(b). We find that the direct band gap of D135 is fairly stable upon the increase of external pressure. This particular pressure dependence of the band gap rules out the possibility that the direct band gap nature of D135 arises from the folding of the Brillouin zone. For D135, as the external pressure exceeds 106 kbar, the band gap changes from direct to indirect. On the contrary, in the cubic diamond case, the indirect band gap size decreases more rapidly with increasing pressure. The band structures of D135, Q135, and I926 calculated by using the PBE exchange-correlation functional are shown in Fig. 7. In D135, the direct band gap with the size of 0.64 eV is located at the Brillouin zone center, while it increases to 1.05 eV in quasiparticle G_0W_0

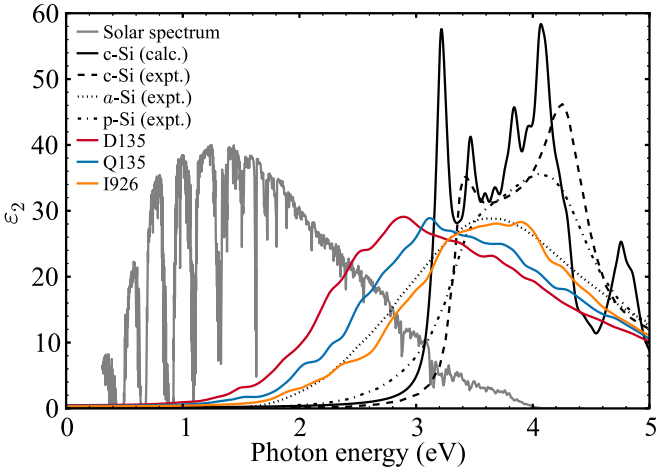

FIG. 8. (Color online) The imaginary part of the dielectric function $\varepsilon_2(\omega)$ is shown as a function of photon energy. Data for D135 (red), Q135 (blue), and I926 (yellow) are shown in color and the solar spectrum (Ref. [37]) in gray. Diamond Si, amorphous Si, and polycrystalline Si are respectively denoted as c-Si, a-Si, and p-Si. The absorption of I926 is shown to be as good as a-Si probably due to rather small difference between the direct and indirect band gaps ($E_g^d - E_g^i = 0.24$ eV).

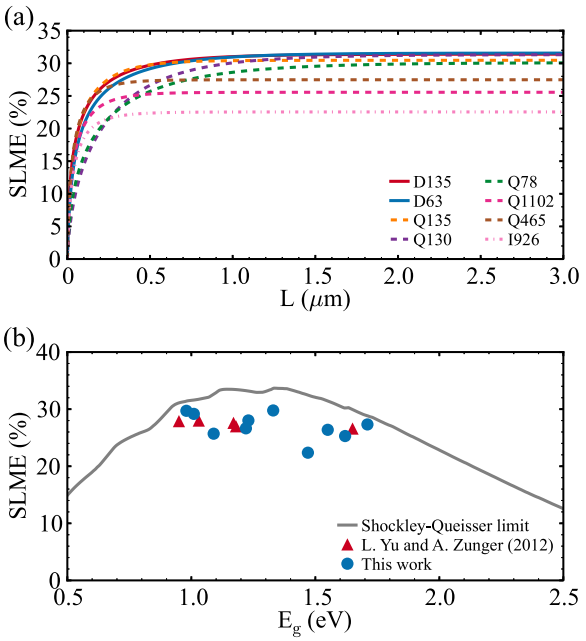

FIG. 9. (Color online) (a) The spectroscopic limited maximum efficiency (SLME) [38] is calculated as the function of film thickness L for D135, D63, Q130, Q135, Q78, Q1102, Q465, and I926. For D135, SLME reaches 29.71% at the film thickness of $L = 0.5$ μm. (b) The photovoltaic efficiency of D135 is shown along with other designed silicon crystals (Table II) and top five systems ($CuInTe_2$, $CuInSe_2$, $AgInTe_2$, $AgInSe_2$, and $CuGaSe_2$) proposed by Yu and Zunger [38]. For comparison, the theoretical upper limit (Shockley-Queisser efficiency limit) is also shown.

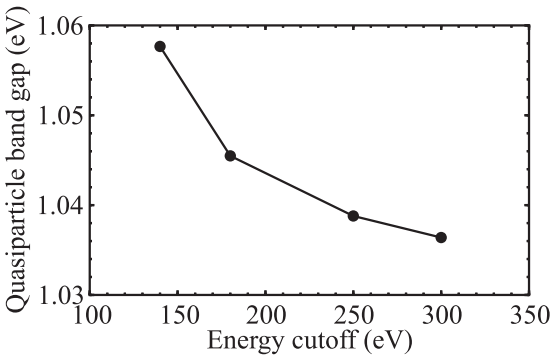

FIG. 10. The variation of the quasiparticle G_0W_0 band gap is plotted with respect to the energy cutoff for D135.

calculations [33]. On the other hand, I926 has the indirect band gap of 1.10 eV, with the valence band edge lying on the Γ-Y symmetry line and the conduction band edge at the N point in the Brillouin zone. With the PBE functional, Q135 reveals the direct gap of 0.93 eV at the Γ point, which is larger by about 0.3 eV than that of D135. However, quasiparticle G_0W_0 calculations show that the conduction band minimum is located at the Y point. Thus, the band gap becomes quasidirect, with the size of 1.31 eV, while the direct gap is 1.40 eV at the Γ point.

To investigate the optical absorption spectrum, which is relevant to photovoltaic absorption, we calculate the imaginary part of the dielectric function $\varepsilon_2(\omega)$ by solving the Bethe-Salpeter equation [34] together with the quasiparticle G_0W_0 approximation [33], as implemented in the VASP code [35,36]. We obtain the numerical convergence of quasiparticle band gaps and optical absorption spectrum by varying various computational parameters, as described in Appendix A. It is

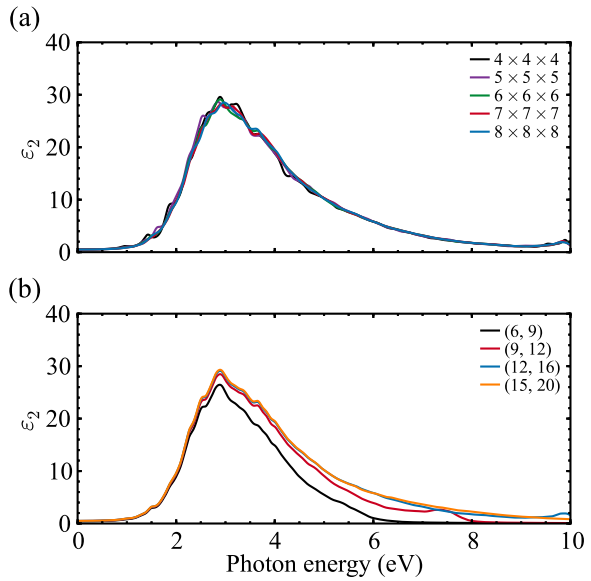

FIG. 11. (Color online) For D135, the variation of the imaginary part of the dielectric function is plotted with respect to (a) the $\vec{k}$-point grid and (b) the number of bands considered in the BSE calculations. In (b), n_1 and n_2 in parentheses (n_1,n_2) denote the numbers of occupied and unoccupied bands around the Fermi level, respectively.

TABLE III. The lattice parameters of the D135, Q135, and I926 structures.

Structure	a (Å)	b (Å)	c (Å)	α (°)	β (°)	γ (°)
D135	13.88	5.69	7.10	90	114.64	90
Q135	14.06	5.66	7.22	90	63.92	90
I926	7.60	7.73	11.84	90	80.96	90

noted that the direct transition gap in absorption spectrum is slightly smaller than the quasiparticle band gap due to the exciton effect (Table II). In Fig. 8, $\varepsilon_2(\omega)$ is shown for D135, Q135, and I926, along with the solar spectrum. Data for various silicon phases including diamond Si, amorphous Si, and polycrystalline Si are also included for comparison. The measured dielectric function via spectroscopic ellipsometry is taken from Ref. [37]. The absorption spectrum of D135 exhibits a significant overlap with the solar spectrum and thus an excellent photovoltaic efficiency, with great improvements over amorphous Si, polycrystalline Si, and diamond Si. In Q135, overall the absorption spectrum shifts by about 0.3 eV toward the higher energy due to the larger band gap. Since the characteristics of dipole-allowed transitions around the Brillouin zone center are similar to those for D135, Q135 still exhibits good solar absorption spectrum. For D135 and Q135, the photovoltaic efficiencies [38] are estimated to be 29.71% and 29.77%, respectively (Table II and Fig. 9). It should be noted that the Shockley-Queisser limit [39] of the solar cell efficiency is 33.7%. On the other hand, the absorption spectrum of I926 is similar to that of amorphous Si. The difference between D135 and I926 in the absorption spectrum clearly indicates that the direct gap of D135 does not simply result from the band-folding effect. Since D135, Q135, and I926 are all crystalline in their structures without coordination defects (Wyckoff positions of atoms are given in Appendix B), they do not suffer from degradation in solar cells, unlike the amorphous Si.

IV. CONCLUSIONS

In conclusion, we have predicted crystalline silicon phases with direct gaps by combining the conformational space annealing (CSA) method for global optimization and the first-principles density functional calculations, and also identified many additional quasidirect gap structures. We have shown that the band gap characteristics of Si can be modified by varying the dihedral-angle distribution while keeping strong and stable covalent bonds between the Si atoms, so that special

TABLE IV. Wyckoff positions of atoms in D135.

Site	Fractional coordinates		
4a	0.761 51	0.225 54	0.815 02
4a	0.513 44	0.356 94	0.336 21
4a	−0.020 03	0.456 10	0.250 93
4a	0.082 46	0.154 20	0.203 16
4a	0.864 88	0.427 73	0.419 62
4a	0.327 74	0.413 92	0.075 04

TABLE V. Wyckoff positions of atoms in Q135.

Site	Fractional coordinates		
8f	0.091 06	0.960 31	0.436 88
8f	0.193 81	0.302 10	0.424 71
8f	0.159 08	0.672 85	0.581 73

TABLE VI. Wyckoff positions of atoms in I926.

Site	Fractional coordinates		
8j	0.697 04	0.251 95	0.204 52
8j	0.417 52	0.261 20	0.324 04
4i	0.882 95	0.000 00	0.447 44
4i	0.603 79	0.000 00	0.565 80
4i	0.366 75	0.000 00	0.896 94
4i	0.685 95	0.000 00	0.899 21

arrangements of the atoms in the unit cell lead to direct gap electronic structures. Our approach opens new perspectives for the inverse design of materials by providing high efficiency in search for superior materials with preassigned properties.

ACKNOWLEDGMENTS

IHL and JL are supported by the National Research Foundation of Korea (NRF) under Grant No. 2008-0061987 funded by the Korea government (MEST). YJO, SK, and KJC are supported by the National Research Foundation of Korea (NRF) under Grant No. NRF-2005-0093845 and Samsung Science and Technology Foundation under Grant No. SSTF-BA1401-08. We thank Korea Institute for Advanced Study (KIAS Center for Advanced Computation) and Korea Institute of Science and Technology Information (Supercomputing Center: KSC-2013-C2-040) for providing computing resources. We thank Steven Gross and Kevin Cahill for their critical comments and suggestions on the manuscript.

APPENDIX A: CONVERGENCE TEST OF QUASIPARTICLE BAND GAP AND OPTICAL ABSORPTION SPECTRUM

We test the numerical convergence of quasiparticle band gap and optical absorption spectrum by varying various computational parameters. It was shown that band gaps vary with the energy cutoff and the numbers of occupied and unoccupied bands used in quasiparticle calculations [40]. The optical absorption spectrum obtained by solving the Bethe-Salpeter equation (BSE) is also sensitive to the numbers of $\vec{k}$ points and bands used. For D135, the quasiparticle band gap and optical absorption spectrum are calculated by using the VASP code (ver. 5.3.3). With the parameters of 180 eV, 180, and $6 \times 6 \times 6$ for the energy cutoff, the number of bands, and the $\vec{k}$-point grid, respectively, the G_0W_0 band gap is accurate to within 0.01 eV. As the energy cutoff increases from 180 to 300 eV, the quasiparticle gap decreases only by 0.01 eV, as shown in Fig. 10. Moreover, the quasiparticle gap remains almost unchanged even if the fine $8 \times 8 \times 8$ $\vec{k}$-point grid is used. We note that the absorption spectrum is sensitive to the numbers of occupied and unoccupied bands in the high energy region above 5 eV, while it is rather insensitive to the $\vec{k}$-point grid (Fig. 11). With the same parameters of 180 eV and $6 \times 6 \times 6$ for the energy cutoff and the $\vec{k}$-point grid, respectively, we find that the absorption spectrum is well converged with the choice of 12 occupied and 16 unoccupied bands around the Fermi level. Therefore our calculations ensure that the solar absorption spectra of the designed materials are properly described for energies below 5 eV.

APPENDIX B: STRUCTURAL INFORMATION ON D135, Q135, AND I926

The lattice parameters and Wyckoff positions of D135, Q135, and I926 are given in Tables III–VI.

[1] B. P. Jelle, C. Breivik, and H. D. Røkenes, Solar Energy Mater. Sol. Cells **100**, 69 (2012).
[2] G. Ceder and K. Persson, Sci. Am. **309**, 36 (2013).
[3] A. Franceschetti and A. Zunger, Nature (London) **402**, 60 (1999).
[4] C. J. Pickard and R. J. Needs, J. Phys.: Condens. Matter **23**, 053201 (2011).
[5] M. Amsler and S. Goedecker, J. Chem. Phys. **133**, 224104 (2010).
[6] Y. Wang, J. Lv, L. Zhu, and Y. Ma, Comput. Phys. Comm. **183**, 2063 (2012).
[7] Q. Li, D. Zhou, W. Zheng, Y. Ma, and C. Chen, Phys. Rev. Lett. **110**, 136403 (2013).
[8] S. Botti, J. A. Flores-Livas, M. Amsler, S. Goedecker, and M. A. L. Marques, Phys. Rev. B **86**, 121204 (2012).
[9] H. J. Xiang, B. Huang, E. Kan, S.-H. Wei, and X. G. Gong, Phys. Rev. Lett. **110**, 118702 (2013).
[10] F. H. Stillinger, Phys. Rev. E **59**, 48 (1999).
[11] J. Lee, I.-H. Lee, and J. Lee, Phys. Rev. Lett. **91**, 080201 (2003).
[12] J. Lee, H. A. Scheraga, and S. Rackovsky, J. Comput. Chem. **18**, 1222 (1997).
[13] J. Lee, J. Pillardy, C. Czaplewski, Y. Arnautova, D. R. Ripoll, A. Liwo, K. D. Gibson, R. J. Wawak, and H. A. Scheraga, Compt. Phys. Comm. **128**, 399 (2000).
[14] K. Joo, J. Lee, S. Lee, J. H. Seo, S. J. Lee, and J. Lee, Proteins: Struct., Funct., Bioinf. **69**, 83 (2007); K. Joo, J. Lee, S. Sim, K. Lee, S. Heo, S. Y. Lee, I.-H. Lee, S. J. Lee, and J. Lee, *ibid.* **82**, 188 (2014).
[15] J. H. Holland, *Adaptation in Natural and Artificial Systems: An Introductory Analysis with Applications to Biology, Control, and Artificial Intelligence*, 2nd ed. (MIT Press, Cambridge, 1992).

[16] P. Hohenberg and W. Kohn, Phys. Rev. **136**, B864 (1964).
[17] J. P. Perdew, K. Burke, and M. Ernzerhof, Phys. Rev. Lett. **77**, 3865 (1996).
[18] G. Kresse and D. Joubert, Phys. Rev. B **59**, 1758 (1999).
[19] G. Kresse and J. Furthmüller, Comput. Mater. Sci. **6**, 15 (1996).
[20] K. Cahill, *Physical Mathematics* (Cambridge University Press, Cambridge, England), Chap. 14.4.
[21] W. Kohn and L. J. Sham, Phys. Rev. **140**, A1133 (1965).
[22] O. O. Kurakevych, T. A. Strobel, D. Y. Kim, T. Muramatsu, and V. V. Struzhkin, Cryst. Growth Desn. **13**, 303 (2013).
[23] R. O. Piltz, J. R. Maclean, S. J. Clark, G. J. Ackland, P. D. Hatton, and J. Crain, Phys. Rev. B **52**, 4072 (1995).
[24] S. Ruffell, J. E. Bradby, N. Fujisawa, and J. S. Williams, J. Appl. Phys. **101**, 083531 (2007).
[25] J. S. Kasper, P. Hagenmuller, M. Pouchard, and C. Cros, Science **150**, 1713 (1965).
[26] I. Štich, R. Car, and M. Parrinello, Phys. Rev. B **44**, 11092 (1991).
[27] I.-H. Lee and K. J. Chang, Phys. Rev. B **50**, 18083 (1994).
[28] J. Fortner and J. S. Lannin, Phys. Rev. B **39**, 5527 (1989).
[29] S. V. Faleev, M. van Schilfgaarde, and T. Kotani, Phys. Rev. Lett. **93**, 126406 (2004).
[30] L. L. Boyer, E. Kaxiras, J. L. Feldman, J. Q. Broughton, and M. J. Mehl, Phys. Rev. Lett. **67**, 715 (1991).
[31] A. Togo, F. Oba, and I. Tanaka, Phys. Rev. B **78**, 134106 (2008).
[32] W. A. Kamitakahara, C. M. Soukoulis, H. R. Shanks, U. Buchenau, and G. S. Grest, Phys. Rev. B **36**, 6539 (1987).
[33] M. S. Hybertsen and S. G. Louie, Phys. Rev. B **34**, 5390 (1986); L. Hedin, J. Phys.: Condens. Matter **11**, R489 (1999).
[34] E. E. Salpeter and H. A. Bethe, Phys. Rev. **84**, 1232 (1951).
[35] F. Fuchs, J. Furthmüller, F. Bechstedt, M. Shishkin, and G. Kresse, Phys. Rev. B **76**, 115109 (2007).
[36] M. J. van Setten, R. Gremaud, G. Brocks, B. Dam, G. Kresse, and G. A. de Wijs, Phys. Rev. B **83**, 035422 (2011).
[37] G. E. Jellison, M. F. Chisholm, and S. M. Gorbatkin, Appl. Phys. Lett. **62**, 3348 (1993).
[38] L. Yu and A. Zunger, Phys. Rev. Lett. **108**, 068701 (2012).
[39] W. Shockley and H. J. Queisser, J. Appl. Phys. **32**, 510 (1961).
[40] B.-C. Shih, Y. Xue, P. Zhang, M. L. Cohen, and S. G. Louie, Phys. Rev. Lett. **105**, 146401 (2010).